

Near-infrared and optical studies of the highly obscured nova V1831 Aquilae (Nova Aquilae 2015)

D. P. K. Banerjee,^{1★} Mudit K. Srivastava,^{1★} N. M. Ashok,¹ U. Munari,²
F.-J. Hambsch,³ G. L. Righetti³ and A. Maitan³

¹*Astronomy and Astrophysics Division, Physical Research Laboratory, Navrangpura, Ahmedabad 380009, India*

²*INAF Astronomical Observatory of Padova, via dell'Osservatorio 8, 36012 Asiago (VI), Italy*

³*ANS Collaboration, c/o Astronomical Observatory, 36012 Asiago (VI), Italy*

Accepted 2017 September 19. Received 2017 September 19; in original form 2016 November 8

ABSTRACT

Near-infrared (NIR) and optical photometry and spectroscopy are presented for the nova V1831 Aquilae, covering the early decline and dust-forming phases during the first ~ 90 d after its discovery. The nova is highly reddened due to interstellar extinction. Based solely on the nature of the NIR spectrum, we are able to classify the nova to be of the Fe II class. The distance and extinction to the nova are estimated to be 6.1 ± 0.5 kpc and $A_V \sim 9.02$, respectively. Lower limits of the electron density, emission measure and ionized ejecta mass are made from a Case B analysis of the NIR Brackett lines, while the neutral gas mass is estimated from the optical [O I] lines. We discuss the cause of the rapid strengthening of the He I 1.0830- μ m line during the early stages. V1831 Aql formed a modest amount of dust fairly early (~ 19.2 d after discovery); the dust shell is not seen to be optically thick. Estimates of the dust temperature, dust mass and grain size are made. Dust formation commences around day 19.2 at a condensation temperature of 1461 ± 15 K, suggestive of a carbon composition, following which the temperature is seen to decrease gradually to 950 K. The dust mass shows a rapid initial increase, which we interpret as being due to an increase in the number of grains, followed by a period of constancy, suggesting the absence of grain destruction processes during this latter time. A discussion of the evolution of these parameters is made, including certain peculiarities seen in the grain radius evolution.

Key words: line: identification – techniques: photometric – techniques: spectroscopic – stars: individual: Nova Aquilae 2015 (V1831 Aquilae) – novae, cataclysmic variables – infrared: general.

1 INTRODUCTION

V1831 Aql was first detected as a new transient source by the All-Sky Automated Survey for Supernovae (ASASSN) and designated as ASASSN-15qj by Shappee et al. (2015) on 2015 September 29.31 UT at $V \sim 14.7$ (error 0.1 mag) under hazy sky conditions. A more robust confirmation was subsequently made at $V = 15.2$ on 2015 October 1.29 UT. An archival search of the Kamogata–Kiso–Kyoto Wide-Field Survey (Shappee et al. 2015 and references within) showed a pre-discovery detection of the source at $I_c = 10.5$ on 2015 September 27.409 UT. Shappee et al. (2015) suggested that the new transient was likely to be a highly obscured galactic nova with the large $E(V - I_c)$ value of ~ 4.6 , suggesting considerable interstellar extinction. The search for the quiescent counterpart of the

nova in the UKIDSS Galactic Plane Survey data base by Maccarone (2015) resulted in the detection of a source with $K = 17.1 \pm 0.1$ (UGPS J192150.15+150924.8) with good positional coincidence. Assuming this source to be the nova progenitor and adopting the required estimates involving the extinction to the nova, the intrinsic colours of cataclysmic variables at quiescence and the distance to the nova, Maccarone (2015) inferred that the absolute magnitude of this potential progenitor should be $M_V \sim 3.8$, making it easily faint enough to have been undetected in pre-outburst optical data. We discuss this further in Section 3.1 when estimating the outburst amplitude of the nova. Close to the Shappee et al. (2015) discovery, V1831 Aql was also detected by Itagaki (Nakano 2015) at an unfiltered magnitude of 12.4 on 2015 October 5.548 UT; the source was designated as PNV J19215012+1509248 = Nova Aquilae 2015. Spectroscopic confirmation of the source as a nova was obtained on 2015 October at 5.598 and 6.482 UT by Maehara & Fujii (2015) and Fujii (2015), who noted the strong H α emission (full width at

* E-mail: orion@prl.res.in (DPKB); mudit@prl.res.in (MKS)

half-maximum (FWHM) = 1600 km s⁻¹) in the spectrum and the presence of emission lines of Fe II (multiplets 73,74), O I, Ca II and [O I]. However, the authors did not attempt to classify whether the nova was of the Fe II or He/N class. This may be due to considerable faintness in the blue part of the spectrum because of high reddening, i.e. very low signal in the blue region, where the strongest of the Fe II lines – generally used to identify Fe II novae – are expected to register. Because the near-infrared (NIR) region is more amenable for observations in directions of high extinction, NIR spectra in the 0.9–2.5 μm region were less affected and these clearly established the nova to be of the Fe II class (Ashok, Srivastava & Banerjee 2015). The Fe II classification was later confirmed by Goranskij & Barsukova (2015) in the optical.

In this article, we present our NIR and optical spectroscopic and photometric observations of V1831 Aql, preliminary reports of which were made in Ashok et al. (2015) and Srivastava, Banerjee & Ashok (2015a).

2 OBSERVATIONS

2.1 Optical photometry and spectroscopy observations

Optical photometry of Nova Aql 2015 was obtained with Asiago Novae and Symbiotic stars (ANS) Collaboration telescopes N. 140, 157, 210 and 220. The nova was observable only in R_c and I_c bands, because of its faintness and extremely red colours. The same local photometric sequence, spanning a wide colour range and carefully calibrated against Landolt (2009) equatorial standards, was used for all telescopes and observing epochs, ensuring a high consistency among different data sets. Table 1 gives the details of R_c - and I_c -band photometry, where the quoted uncertainties represent the total error budget, which combines the measurement error of the variable quadratically with the error associated with transformation from the local to the standard photometric system (as defined by the photometric comparison sequence around the nova linked to Landolt's standards). The operation of ANS Collaboration telescopes is described in detail by Munari et al. (2012) and Munari & Moretti (2012). They are all located in Italy. All measurements on the programme nova were carried out with aperture photometry. Colours and magnitudes are obtained separately during the reduction process and are not derived from one another.

Low-resolution 3300–8000 Å spectra of V1831 Aql were obtained with the 1.22-m telescope + B&C spectrograph operated in Asiago by the Department of Physics and Astronomy of the University of Padova. The CCD camera is an ANDOR iDus DU440A with a back-illuminated E2V 42-10 sensor and 2048 × 512 array of 13.5-μm pixels. Low- and medium-resolution 5600–10 200 Å spectra of V1831 Aql were obtained with the Asiago Faint Object Spectrograph and Camera (AFOSC) spectrograph and imager mounted on the 1.82-m telescope operated in Asiago by the INAF Astronomical Observatory of Padova. The CCD camera is an Andor DW436-BV, which houses an E2V CCD42-40 AIMO back-illuminated CCD as detector, and the dispersing elements are VPH gratings. Finally, a high-resolution spectrum of V1831 Aql was recorded at a resolving power of 20 000 with the Echelle spectrograph mounted on the Asiago 1.82-m telescope. Table 2 provides a log of the spectroscopic observations.

2.2 NIR observations from Mount Abu

Nova Aql 2015 was observed with the 1.2-m optical/NIR telescope of the Physical Research Laboratory at Mount Abu Infrared ob-

Table 1. Log of the optical photometry.

Date (UT) (yyyy-mm-dd)	Time ^a (days)	R_c (mags)	I_c (mags)	Tel. ^b
2015-10-08.82	9.32	13.300 ± 0.016	11.240 ± 0.013	220
2015-10-11.80	12.30	13.404 ± 0.018	11.344 ± 0.019	220
2015-10-11.88	12.38	13.469 ± 0.011	11.404 ± 0.006	157
2015-10-12.07	12.56		11.413 ± 0.010	210
2015-10-13.07	13.57		11.485 ± 0.010	210
2015-10-14.07	14.57		11.374 ± 0.013	210
2015-10-15.07	15.57		11.456 ± 0.011	210
2015-10-16.07	16.57		11.653 ± 0.015	210
2015-10-19.78	20.28	14.005 ± 0.012	11.966 ± 0.006	157
2015-10-20.81	21.31	14.001 ± 0.011	11.895 ± 0.005	157
2015-10-21.05	21.55		12.021 ± 0.019	210
2015-10-21.74	22.24	14.124 ± 0.011	11.981 ± 0.005	157
2015-10-22.05	22.55		11.981 ± 0.021	210
2015-10-23.05	23.55		12.091 ± 0.022	210
2015-10-23.84	24.34	14.317 ± 0.015	12.216 ± 0.010	157
2015-10-24.75	25.25	14.367 ± 0.016	12.289 ± 0.010	157
2015-10-30.74	31.24	14.799 ± 0.020	12.757 ± 0.010	157
2015-10-31.75	32.25	14.772 ± 0.024	12.828 ± 0.027	220
2015-10-31.77	32.27	14.892 ± 0.014	12.822 ± 0.010	157
2015-11-01.79	33.29	14.858 ± 0.020	12.912 ± 0.021	220
2015-11-02.73	34.23	15.152 ± 0.019	13.030 ± 0.012	157
2015-11-02.79	34.29	15.080 ± 0.025	13.128 ± 0.018	220
2015-11-06.73	38.23	15.480 ± 0.027	13.417 ± 0.011	157
2015-11-08.73	40.23	15.646 ± 0.016	13.589 ± 0.010	157
2015-11-08.75	40.25	15.452 ± 0.015	13.510 ± 0.012	220
2015-11-12.00	43.50		13.761 ± 0.047	210
2015-11-13.01	44.51		13.952 ± 0.055	210
2015-11-15.01	46.51		14.173 ± 0.300	210
2015-11-16.01	47.51		13.742 ± 0.043	210
2015-11-17.01	48.51		13.999 ± 0.065	210
2015-11-18.01	49.51		14.184 ± 0.062	210
2015-11-20.01	51.51		13.932 ± 0.054	210
2015-11-21.01	52.51		14.089 ± 0.073	210
2015-11-22.72	54.22	16.513 ± 0.049	14.790 ± 0.029	220
2015-11-27.73	59.23	16.554 ± 0.041	14.882 ± 0.019	220
2015-12-10.75	72.25	16.650 ± 0.030	15.732 ± 0.032	140
2015-12-21.69	83.19	17.110 ± 0.032	16.290 ± 0.030	140

^aMeasured from JD2457295.00 (2015-09-29.50) = t_0 .

^bTelescope number of the ANS consortium.

Table 2. Log of the optical spectroscopic observations from Asiago.

Date (UT) (yyyy-mm-dd)	Time (days)	Exp. time (s)	Range (nm)	Å pixel ⁻¹	Instrument & Telescope
2015-10-16.80	17.30	240	330–800	2.31	B&C, 1.22m
2015-10-20.84	21.34	480	330–800	2.31	B&C, 1.22m
2015-10-23.81	24.31	600	330–800	2.31	B&C, 1.22m
2015-10-23.85	24.35	1800	370–740		Echelle, 1.82m R = 20,000
2015-11-03.77	35.28	1200	330–800	2.31	B&C, 1.22m
2015-11-06.72	38.22	1800	330–800	2.31	B&C, 1.22m
2015-11-24.74	56.24	900	330–800	2.31	B&C, 1.22m
2015-12-10.71	72.21	1800	624–696	0.39	AFOSC, 1.82m
2015-12-10.74	72.24	1800	560–1020	2.95	AFOSC, 1.82m

servatory, India using the Near-Infrared Camera and Spectrometer (NICS). NICS contains a re-imaging optical chain, along with a 1024 × 1024 HgCdTe Hawaii array as detector. It provides a resolution of ~1000 in spectroscopy mode and covers J , H and K_s wavelength bands from 0.85–2.4 μm. Three different orientations

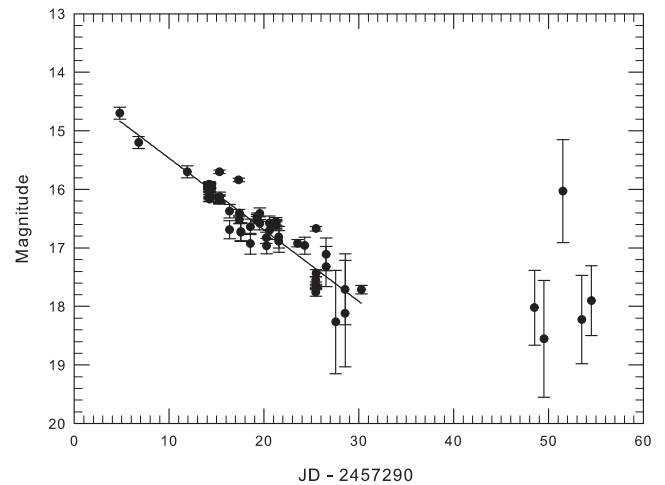
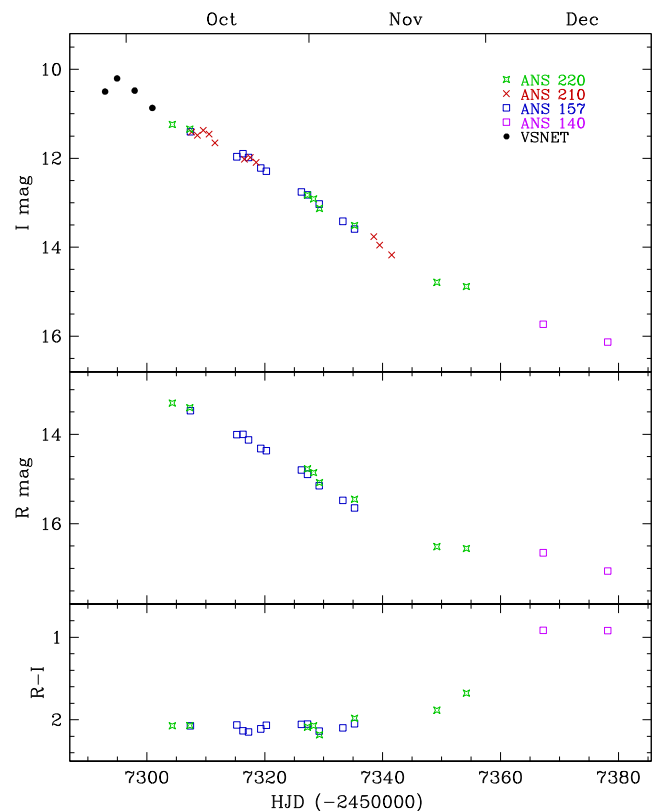
Table 3. Log of the NIR spectroscopy from Mount Abu.

Date (UT) (yyyy-mm-dd.dd)	Time (days)	Exposure time (s) (IJ, JH, HK)	Std. star
2015-10-08.75	9.25	(300, 240, 240)	SAO 104779
2015-10-16.72	17.22	(600, 480, 480)	SAO 104779
2015-10-17.68	18.18	(600, 600, 600)	SAO 104779
2015-10-18.71	19.21	(600, 600, 600)	SAO 104779
2015-10-19.72	20.22	(600, 600, 600)	SAO 104779
2015-10-26.65	27.15	(—, 540, 600)	SAO 104779
2015-10-27.67	28.17	(600, 600, 600)	SAO 104779
2015-11-04.68	36.18	(300, 360, 360)	SAO 104779
2015-11-05.60	37.10	(600, 600, 600)	SAO 104779
2015-11-19.63	51.13	(380, 760, 760)	SAO 104779
2015-11-26.61	58.11	(380, 760, 760)	SAO 104804
2015-11-27.62	59.12	(—, 380, 760)	SAO 104804
2015-12-02.57	64.07	(380, 760, 760)	SAO 104804
2015-12-18.56	80.06	(380, 380, 760)	SAO 104804

Table 4. Log of the NIR photometry from Mount Abu.

Date (UT) (yyyy-mm-dd.dd)	Time (days)	<i>J</i> (mag)	<i>H</i> (mag)	<i>K_s</i> (mag)
2015-10-08.79	9.29	8.32 ± 0.05	7.75 ± 0.03	7.09 ± 0.04
2015-10-16.76	17.26	8.92 ± 0.06	8.18 ± 0.04	7.12 ± 0.07
2015-10-17.72	18.22	8.90 ± 0.07	8.12 ± 0.11	6.91 ± 0.06
2015-10-18.75	19.25	8.97 ± 0.08	8.13 ± 0.02	6.89 ± 0.10
2015-10-19.76	20.26	9.13 ± 0.04	8.02 ± 0.05	—
2015-10-26.69	27.19	9.18 ± 0.06	7.38 ± 0.05	5.76 ± 0.05
2015-10-27.71	28.21	9.15 ± 0.08	7.32 ± 0.03	5.71 ± 0.05
2015-11-04.72	36.22	9.29 ± 0.04	7.20 ± 0.04	5.26 ± 0.11
2015-11-05.64	37.14	9.40 ± 0.04	7.33 ± 0.06	5.57 ± 0.05
2015-11-20.63	52.13	10.36 ± 0.06	8.08 ± 0.04	6.14 ± 0.05
2015-12-01.58	63.08	11.10 ± 0.04	8.73 ± 0.02	6.69 ± 0.02
2015-12-17.56	79.06	11.83 ± 0.07	9.65 ± 0.10	7.46 ± 0.07
2015-12-19.56	81.06	11.91 ± 0.03	9.74 ± 0.02	7.61 ± 0.08
2015-12-25.54	87.04	12.20 ± 0.05	—	8.00 ± 0.05

of NICS gratings are used to record spectra in *IJ*, *JH* and *HK* regions with suitable overlaps. Photometry and spectroscopy of Nova Aql 2015 were performed using NICS for a total of 19 epochs from 2015 October 8–2016 December 25. For telluric line corrections in the spectra of Nova Aql 2015, spectra of a standard star (SAO 104779/FI V spectral class and SAO 104804/A0 spectral class; details are given in Table 3) were also taken at similar airmass. All the spectra were obtained in two dithered positions of the objects along the slit. Dark and sky-line corrected spectral frames were obtained by subtracting one from the other. The data were later reduced using self-developed image processing codes in *c* with *fit-sio* library functions and *IRAF* tasks. Wavelength calibrations were applied by identifying OH sky lines and telluric lines. Several sets of reduced spectra were then co-added. The standard star spectra showed the presence of hydrogen Paschen and Brackett lines. These lines were identified and removed. Nova spectra were then ratioed with these cleaned standard star spectra and multiplied further by the blackbody distribution function corresponding to the effective temperature of the standard star. Aperture photometry of Nova Aql 2015 in *J*, *H* and *K_s*, along with photometric standard stars, was performed to estimate magnitudes following standard procedures (e.g. Banerjee & Ashok 2002). The details of the NIR observations are given in Tables 3 and 4.


Figure 1. The V-band light curve from AAVSO data. A linear fit to the segment of observed data used to estimate t_2 is shown. Additional details of the light curve are discussed in the text.

Figure 2. The light curves in the R_c and I_c bands from data collected by different telescopes (shown by different symbols) of the ANS consortia, Italy. The halt of the decline in the R_c band around JD 7350 is due to the emerging dominance of Balmer $H\alpha$, which declines more slowly than the continuum.

3 RESULTS

3.1 Light curve, extinction, distance and outburst amplitude

The V-band light curve from AAVSO data is presented in Fig. 1, while the R_c - and I_c -band light curves are shown in Fig. 2. The

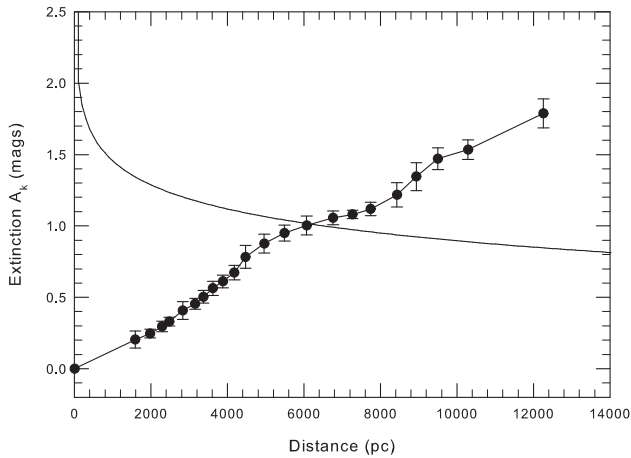


Figure 3. The curve joining the data points (black circles) shows the variation of the extinction towards V1831 Aquilae based on results from Marshall et al. (2006). The continuous straight line is a plot of extinction A versus distance d from the equation $m_v - M_v = 5 \log d - 5 + A_v$, where m_v is known from observations and M_v is estimated from MMRD relations. The intersection of the two curves permits simultaneous estimation of the extinction and distance to the nova. More details are given in the text.

absolute magnitude M_v of the nova is estimated from the maximum magnitude versus rate of decline (MMRD) relations given by della Valle & Livio (1995) and Downes & Duerbeck (2000). These relations correlate the absolute magnitude M_v with the time to decline by two magnitudes from visual maximum (t_2), which is a measure of the speed class of a nova. To estimate t_2 , four discrepant data points had to be excluded from the AAVSO light curve. These rejected points were isolated outliers and obviously erroneous, lying as much as ~ 2 – 2.5 mag away from their neighbouring data. Fig. 1 also includes a few reported magnitudes from Shappee et al. (2015) and Nakano (2015). A least-squares minimized linear fit to the data gives $t_2 = 16.4 \pm 0.5$ d, assuming 2015 September 29.5 as the time of optical maximum as inferred from the I_c light curve of Fig. 2. In all subsequent discussion, we take 2015 September 29.5 UT as the reference time (t_0). $t_2 = 16.4 \pm 0.5$ d puts this nova in the fast speed class (Payne-Gaposchkiin 1957 and references therein). We discuss the expected time-scale for dust formation in novae of this speed class (Williams et al. 2013) at a later stage. Adopting $m_v(\text{max}) = 14.7$ (Shappee et al. 2015) yields a value of the absolute magnitude of $M_v = -8.29 \pm 0.20$ from the MMRD relation of della Valle & Livio (1995). The MMRD relation of Downes & Duerbeck (2000) gives a consistent value of $M_v = -8.22 \pm 0.83$.

We estimate the extinction and distance to the nova in the following way. If a reliable extinction versus distance plot is available in the nova’s direction (e.g. such as the Marshall et al. (2006) data shown in Fig. 3) and a valid MMRD relation for the nova is also available, then estimates of both the extinction and distance can be made simultaneously. The continuous curve in Fig. 3 shows the A_k versus distance curve from the relation $m_v(\text{max}) - M_v = 5 \log d - 5 + A_v$, wherein we use $m_v(\text{max}) = 14.7$, $M_v = -8.3$ and convert A_v to A_k using $A_k = 0.112A_v$ (Rieke & Levofsky 1985). The second curve in Fig. 3 is the extinction versus distance plot from Marshall et al. (2006) based on modelling of the galactic extinction. The intersection of both curves should give the nova’s distance and extinction, because both curves in principle make use of the same extinction. In the present case, we obtain $d = 6.1 \pm 0.5$ kpc and $A_k = 1.01 \pm 0.03$.

Using $A_k/A_v = 0.112$ and $A_v = 3.09E(B - V)$ (Rieke & Levofsky 1985), we obtain $A_v = 9.02$ and $E(B - V) = 2.92$. We adopt this value of reddening in future calculations. Shappee et al. (2015) derive a larger value of $A_v = 11.5$ compared with our estimate $A_v = 9.02$. Possible ways of reconciling this difference may be as follows. They assume the nova’s intrinsic colours at around maximum to be $(B - V) = (V - I) = 0$, whereas novae at maximum are statistically expected to have an intrinsic $(B - V)$ colour at maximum of 0.23 ± 0.06 , with a 1σ dispersion of 0.16 mag (van den Bergh & Younger 1987). Indeed, novae do show colours between A and F spectral types at maximum (Gehrz 1988). For example, V1500 Cyg at maximum showed $T(\text{eff}) = 6670$ K (Gehrz 1988), corresponding to F4–F5 spectral types, which have an intrinsic $V - I$ colour of ~ 0.5 . Thus their estimate that $E(V - I) = 4.6$ around maximum could have substantial uncertainty. (They derive this using $V = 15.2 \pm 0.1$ from 2015 Oct 01.29 and $I_c = 10.6 \pm 0.1$ from a day later on 2015 Oct 02.4356. Note the large errors in V and I_c .) Thus $E(V - I_c) = 4.6$ could be substantially overestimated, leading to inflated A_v values via their use of the equation $A_v/E(V - I_c) = 2.49$ (Stanek 1996). On the other hand, a lacuna in the approach we have adopted is that the Marshall et al. (2006) extinction curve we used is averaged over a 5 -arcmin² field and not exactly in the direction of the nova. However, extinction can be very patchy and varies considerably over this field; thus the possibility that we have underestimated A_v cannot be ruled out.

One may like to compare the Marshall et al. (2006) extinction data in Fig. 3 with other independent estimates. The Marshall et al. (2006) plot in Fig. 3 shows that extinction in the direction of the nova, up to the maximum distance $d = 12.26$ kpc for which it could be modelled, is $A_k = 1.79 \pm 0.10$. In comparison, Schlafly & Finkbeiner (2011) give a mean value of $A_k \sim 2.09$ along the entire line of sight in the nova’s direction, so the agreement is reasonable.

Novae, considering all speed classes, are found to have a mean absolute magnitude in quiescence between 3.4 and 4.2 mag; fast novae in particular are expected to have a mean absolute magnitude of 3.7 (Warner 1995). Adopting this mean quiescent value of $M_v = 3.7$ as reasonably representative for nova V1831 Aql and using $d = 6.1 \pm 0.5$ kpc and $A_v = 9.02$ as determined earlier, the quiescent apparent magnitude of the nova is expected to be 26.6 ± 0.2 mag. At this level of faintness, the progenitor is not expected to be seen in the optical archival images (also refer to Maccarone 2015). Since maximum brightness was at $m_v = 14.7$ (Shappee et al. 2015), the outburst amplitude is estimated to be ~ 12 mag. That places it at a conventional position, frequented by other classical novae (CNe), in the amplitude of the outburst versus t_2 plot of CNe by Warner (1995, their fig. 5.4).

A few comments may be made regarding the evolution of the $R_c - I_c$ colours shown in the bottom panel of Fig. 2. It must be noted that both R_c - and I_c -band continuum fluxes are greatly affected by the presence of very strong lines covered by the respective filters. There is the $H\alpha$ line in the R_c band and similarly the $O \text{ I } 7774$, 8446 -Å lines in the I_c band. Although the $O \text{ I } 8446$ -Å line is not covered in most of our spectra (except for the 2015 December spectrum) and we can only speculate about its exact contribution to the continuum on other days, it is certainly expected to be stronger than $O \text{ I } 7774$ Å (which is already strong), because of an additional contribution from the $\text{Ly}\beta$ fluorescence presence. $O \text{ I } 8446$ Å is a strong line in novae and the $O \text{ I } 8446/7774$ line ratio in Fe II novae can easily extend from unity to a value of a few times ten (Williams 2012, table 1 therein). Thus, unless fluxed spectra are available at each photometric point to assess the contribution of the $H\alpha$ and $O \text{ I}$ lines to the broad-band fluxes, it becomes difficult to

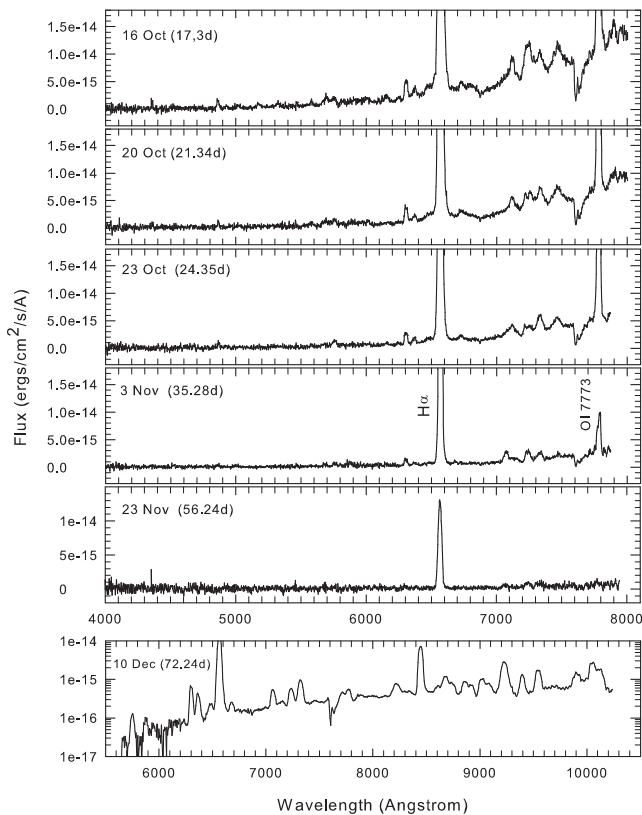


Figure 4. Optical spectra of V1831 Aql at selected epochs. Observation dates are indicated, as well as the days after maximum, which are shown in brackets.

deconstruct and interpret the $R_c - I_c$ colour evolution. One may cautiously conjecture that the increasing trend of the $R_c - I_c$ colour from JD 245 7350 onwards is due to a dominating contribution from the Balmer $H\alpha$ line, the strength of which can decline more slowly than the continuum itself (Munari et al. 2015).

3.2 Optical spectroscopy

The low-resolution optical spectra are presented in Fig. 4. The rise of the continuum in Fig. 4 towards the red shows the large reddening towards the object, which also manifests itself at the blue end of the spectrum, where the signal in the emission features is suppressed considerably. An expanded view of selected regions of the spectra of 2015 October 16 and 2015 November 6 (these have the highest signal-to-noise ratio (S/N)), after a five-point boxcar smoothing to suppress noise and enhance visibility of weak lines, is shown in Fig. 5. In the top panel of Fig. 5, lines of the Fe II (42) and (48) multiplets are seen clearly, thereby establishing the nova to be of the Fe II class. The middle panel, for the same date, looks at the region around $H\alpha$. Here again lines of Fe II and C II are seen, very typical of the Fe II class of novae, and no helium or nitrogen lines typical of Williams’s (1992) He/N type are seen. Under sufficient magnification, many weak lines are seen better, indicating that the spectra of October are closely similar to that of a typical Fe II nova around maximum light and early decline (e.g. there is a good similarity with the spectra of the Fe II nova V977 Sco shown in fig. 5 of Williams et al. 1991). The bottom panel of Fig. 5 plots the same region as the middle one, to highlight the disappearance of Fe II and C II lines and show the emergence of He I and N II lines, indicative of evolution towards higher ionization conditions, as typ-

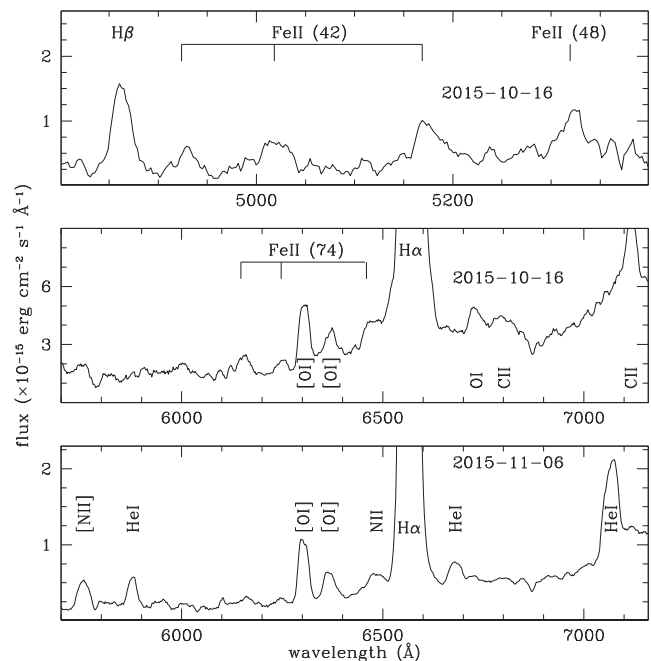


Figure 5. Magnified view of selected sections of the optical spectra to establish the Fe II class of the nova and also show a few other spectral characteristics discussed in the text.

ical of Fe II novae. The appearance of the auroral [N II] 5755-Å line always precedes the emergence of the nebular [N II] 6548, 6584-Å doublet. Whether this doublet is already present in emission we cannot say from this spectrum, given the large width of $H\alpha$, the wings of which overlap and extend beyond the position of the doublet. The [O II] 7319, 7330-Å auroral lines, which generally accompany the [N II] 5755-Å line, can also be seen in the spectrum of 2015 December 10 (Fig. 4, bottom panel). The strongest non-hydrogen line, through the evolution shown here, has been an oxygen line. It is either the O I 7774-Å line or the Lyman β fluoresced 8446-Å O I line. Thus, following the spectral phase classification scheme proposed by Williams et al. (1991), an appropriate spectral phase that could be assigned to the nova over the evolution shown here would be P_0 . It is difficult to comment on the additional spectral features, considering the very low SNR of the spectra of this faint nova.

A high-resolution ($R = 20\,000$) echelle spectrum of the $H\alpha$ line is presented in Fig. 6. The half-width at zero intensity (HWZI) of the line is ~ 2000 km s $^{-1}$, which agrees with its Fe II type. As per the classification scheme of Williams (1992), the observed HWZIs of Fe II novae are generally < 2500 km s $^{-1}$, while for the He/N class it is > 2500 km s $^{-1}$. Correlations are known to exist between the outflow velocities of the ejecta and the speed class. McLaughlin (1960) gives, for the velocity v of the principal ejecta, the relation $\log(v) = 3.57 - 0.5 \times \log t_2$, which for $t_2 = 16.4 \pm 0.5$ d yields an expansion velocity of 917 ± 13 km s $^{-1}$. This is smaller than the observed FWHM of 1300 km s $^{-1}$. On the other hand, studies of novae in M31 by Shafter et al. (2011) yield a similar relation, namely $\log t_2(d) = (6.84 \pm 0.10) - (1.68 \pm 0.02) \log(\text{FWHM}_{H\alpha})$, which leads to an FWHM value of 2230 ± 270 km s $^{-1}$ for the given t_2 . This is on the higher side compared with what is observed. The difference between the observed and outflow velocities inferred from the two empirical laws may be reconciled, in part at least, by a combination of factors. As Shafter et al. (2011) point out, a major factor in the discrepancy between their results and those of McLaughlin (1960) is

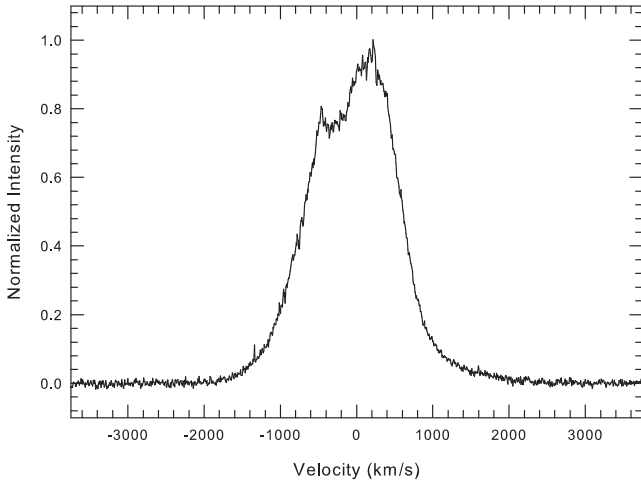


Figure 6. The velocity profile of the $H\alpha$ 6563-Å line on 2015 October 23.85 obtained at a resolution of 20 000. The FWHM of the profile is 1300 km s^{-1} .

that in the latter relation the expansion velocities are derived from the absorption-line minima of the P Cyg profiles measured near maximum light. Such velocities, Shafter et al. (2011) point out, are only 20–50 per cent of those inferred from the emission-line FWHM. On the other hand, Shafter et al. (2011) attribute the scatter in their data, particularly for slower novae, as probably arising in part from the time dependence of the derived velocities, which were obtained from spectra taken at varying times after outburst.

The low-resolution spectra are useful to determine the neutral O I gas mass and temperature. Williams (1994) has shown that the observed flux ratio $I(6300)/I(6364)$ of the forbidden lines of neutral O I is invariably smaller than the value of 3:1 expected from their transition probabilities if these lines were optically thin. This suggests that the O I lines are optically thick, which is not expected based on the relatively small abundance of neutral oxygen in the ejecta and the relevant atomic parameters for the line transitions. The neutral O I, it is therefore suggested, must reside mostly in dense globules, where it is protected from the harsh ionizing radiation from the central white dwarf. Following Williams (1994), the optical depth τ of the [O I] 6300-Å line, the temperature T_e of the neutral gas and the mass M_{O_1} of the neutral O I, respectively, can be found by applying the following three equations in succession:

$$\frac{I_{6300}}{I_{6364}} = \frac{1 - e^{-\tau}}{1 - e^{-\tau/3}}, \quad (1)$$

$$T_e = \frac{11\,200}{\log(43 \times R \times \frac{\tau}{1 - e^{-\tau}})} \text{ K}, \quad (2)$$

$$M_{O_1} = 152d^2 e^{22850/T_e} \times 10^{1.05E(B-V)} \frac{\tau}{1 - e^{-\tau}} I(6300) M_{\odot}, \quad (3)$$

where R is the observed $I(6300)/I(5577)$ flux ratio and d is the distance in kiloparsecs (kpc). Because the measurement of the strength of the 5577-Å line is prone to error, due to its weakness, we have limited our analysis to the spectrum of 2015 October 16, in which this line is best seen. From the spectrum, after correcting for reddening using $E(B - V) = 2.92$, we measure $I(6300)/I(6364) = 1.86 \pm 0.10$ and $I(6300)/I(5577) = 1.62 \pm 0.43$ (reddening corrections were made using $A(5577) = 0.9831A_v$, $A(6300) = 0.8585A_v$ and $A(6364) = 0.8485A_v$ from Cardelli, Clayton & Mathis 1989). This yields $\tau = 1.77 \pm 0.24$, $T_e = 5156 \pm 170 \text{ K}$ and $M_{O_1} = (8.8 \pm 2.2) \times 10^{-5} M_{\odot}$. These values agree well with the list of tabulated values for a large number of novae given by Williams (1994).

3.3 Results from near-infrared observations

The log of the spectroscopic observations is shown in Table 3. The evolution of this nova can be broadly divided, for ease of discussion, into two phases. An early phase comprises the spectra between 2015 October 8 and 19. Spectra subsequent to this belong to a phase that is dominated by emission from dust.

3.3.1 Early-phase spectra

Clear evidence for dust nucleation in the nova was seen by the end of 2015 October. Two representative spectra are shown in Fig. 7, with the principal lines identified. A more detailed identification table can be found in Das et al. (2008) and Banerjee & Ashok (2012), where templates of the NIR spectra of several Fe II and He/N novae are given. The spectra are typical of the Fe II class where, apart from prominent lines of H I, O I and He I, several strong lines of neutral carbon are seen. These lines, which distinguish the Fe II from the He/N class of nova in the infrared, made the Fe II classification a simple exercise in the present case, in an instance where an optical classification was relatively difficult. The $\text{Pa}\beta$ and $\text{Br}\gamma$ H I lines have FWHMs of $1300\text{--}1350 \text{ km s}^{-1}$, after deconvolving for instrument broadening, which matches well the FWHM of 1300 km s^{-1} obtained from the high-resolution $H\alpha$ echelle profile. Among other notable features of the spectra is the presence of neutral Na I lines (e.g. 2.2056 and 2.2084 μm), which have inevitably preceded dust formation (see Das et al. 2008). In this instance, too, dust did indeed form in the nova.

No first-overtone CO emission bands at 2.29 μm and beyond were seen in any of the spectra. From the known first-overtone CO detections in novae, compiled in Banerjee et al. (2016), CO emission in novae is generally seen during the first 1–3 weeks after outburst commencement. CO emission is a transient and short-lived phase that generally does not last more than two weeks (Banerjee et al. 2016 and references therein), consistent with theoretical models for CO formation in nova winds (Pontefract & Rawlings 2004). The transient nature of the emission (Das, Banerjee & Ashok 2009) makes it easy to miss and it is possible, though we deem it unlikely, that CO was formed and destroyed in this nova during the gaps in our observations (e.g. during the first 17 d after discovery, when we have only two epochs of spectroscopic data separated by $\sim 8\text{--}9$ d). All novae known to have shown CO emission have invariably proceeded to form dust, but the converse is not true. Dust has formed in novae where there has been no CO formation. An example is the bright nova V1280 Sco, which formed copious dust (Das et al. 2008; Chesneau et al. 2008, 2012), but where no CO emission was detected. NIR spectroscopic observations of V1280 Sco up till the dust-forming stage were taken at high and sufficiently regular cadence to detect CO, had it formed notwithstanding its transient nature (Das et al. 2008).

3.3.2 Electron density, emission measure and mass estimate

We measured the dereddened Brackett line strengths for the spectrum of 2015 October 8 and performed a Case B analysis. This spectrum was chosen because dust formation is unambiguously absent at this stage; the measured H line strengths are thus not complicated by any effects/contribution from dust emission. Since the analysis presented here is identical to that performed for novae Nova Sco 2015 and Nova Cep 2014 (Srivastava et al. 2015b), the details of the present analysis are not elaborated upon; rather the main findings are summarized. The $\text{Br}\gamma$ 2.1656- μm line is found to be optically

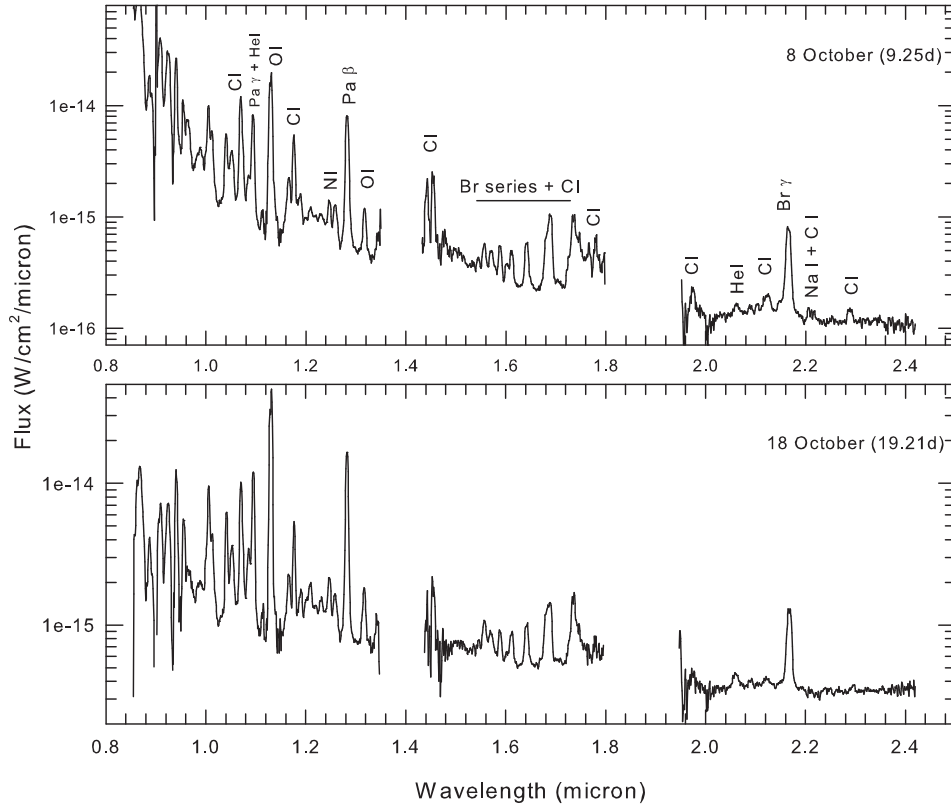


Figure 7. Two representative spectra from the early stage with the prominent lines marked.

thick, as its strength with respect to other Br lines (Br 12–16) deviates from Case B predictions for any reasonable combination of temperature T and electron density n_e . For example, the $\text{Br}\gamma/\text{Br}14$ ratio is found to be 4.15 ± 0.22 , whereas the expected Case B value is 7.63 ± 2.50 when averaged over three different temperatures of 5000, 10 000 and 20 000 K and considering an extended density range between 10^8 and 10^{14} cm^{-3} for each temperature. Even when the temperatures are considered separately, the observed $\text{Br}\gamma/\text{Br}14$ ratio is significantly lower than the expected Case B values. The high density range is considered because high values of the density are expected in the ejecta just 9.25 d after the eruption. Given that nova shell masses are typically estimated to be in the range 10^{-4} – $10^{-6} M_\odot$ (e.g. Gehrz 1988; Della Valle et al. 2002), it is straightforward to show that, during the early stages after outburst, n_e must be high and lie in the middle of the extended range considered. We use the constraint that the optical depth at the line centre of the $\text{Br}\gamma$ line $\tau_{(\text{Br}\gamma)}$ is greater than 1, where, following Hummer & Storey (1987) and Storey & Hummer (1995),

$$\tau_{(\text{Br}\gamma)} = n_e n_i L \Omega_{(\text{Br}\gamma)} > 1, \quad (4)$$

where n_e , n_i , L and $\Omega_{(\text{Br}\gamma)}$ are the electron number density, ion number density, path length and $\text{Br}\gamma$ line opacity, respectively. L is taken as the kinematical distance $v \times t$ travelled by the ejecta, where v is the velocity of ejecta (assumed equal to 650 km s^{-1}) and $t = 9.25 \text{ d}$ is the time after discovery. As $\tau_{(\text{Br}\gamma)}$ can be > 1 , the lower limit on the electron density n_e is found to be in the range $\sim 5 \times 10^9$ – $1.2 \times 10^{10} \text{ cm}^{-3}$ (assuming $n_e = n_i$) and the emission measure $\sim 4.5 \times 10^{33} \text{ cm}^{-5}$. The gas mass of the ejecta may be estimated by $M = \epsilon V n_e m_H$, where V is the volume ($= 4/3\pi L^3$), ϵ is the volume filling factor and m_H is the proton mass. Using the

lower limits on n_e as estimated above, the lower limit on the mass M varies in range $(2.4\text{--}5.7) \times 10^{-6} M_\odot$, assuming $\epsilon = 1$.

3.3.3 The He I 1.0830- μm line strength evolution with respect to the Pa γ 1.094- μm line

One of the striking features of the NIR spectra is the rapid evolution of the (He I 1.083)/(Pa γ 1.094) ratio (denoted by R henceforth) during the early stages. This evolution is shown in Fig. 8 and Table 5. The He I 1.0830- μm line strength strengthens rapidly and the sharp increase in the value of R , specifically between 20 and 28 d, when it changes from 0.31 to 2.4, is quite remarkable. The early evolution of a large number of novae of the Fe II class has been followed from Mount Abu (Banerjee & Ashok 2012 and references within), but we have not encountered a case where the He I 1.0830- μm line brightens so rapidly and persists at a high intensity at such an early stage after outburst. The only exception was nova V574 Pup, but this can be explained by the consideration that it was a hybrid nova (Naik et al. 2010) of the Fe IIb type (Williams 1992), where strong He emission is expected after the transition from the Fe II to the He/N class has been made (strong He lines are expected by definition in He/N class novae). V574 Pup made such a transition approximately a month after its outburst. Having said the above, it should also be mentioned that He I 1.0830- μm can become the strongest line in the NIR spectrum by a very large margin with respect to other lines, but *only* during the later nebular and coronal stages. Examples of such novae, with overwhelmingly strong He I 1.0830 in emission, are PW Vul (Williams, Longmore & Geballe 1996), V574 Pup (Naik et al. 2010), Nova Mon 2012

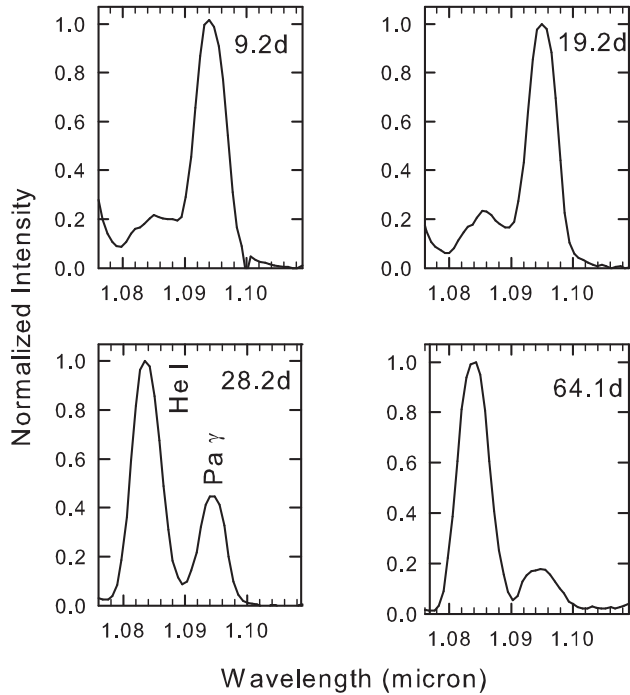


Figure 8. The evolution in the strengths of the He I 1.083- μm and Pa γ 1.094- μm line with time after discovery indicated in days.

Table 5. Evolution of the (He I 1.083- μm)/(Pa γ 1.094- μm) and (He I 2.058- μm)/(Pa γ 1.094- μm) line-strength ratios.

Date of Observation (dd/mm/yy)	Time (days)	(He I 1.083)/(Pa γ 1.094) ratio	(He I 2.058)/(Pa γ 1.094)
08/10/16	9.25	0.31	0.01
16/10/16	17.22	0.28	0.04
17/10/16	18.18	0.25	0.02
18/10/16	19.21	0.32	0.02
19/10/16	20.22	0.31	0.01
27/10/16	28.17	2.40	0.16
04/11/16	35.18	4.78	0.19
05/11/16	36.18	5.38	0.06
19/11/16	51.13	7.19	0.28
26/11/16	58.11	5.55	0.07
02/12/16	64.07	5.45	0.20

(Banerjee, Ashok & Venkataraman 2012) and V5668 Sgr (Banerjee et al. 2016; Gehrz et al. 2016).

In PW Vul, the ratio R increased by a factor of about 70 from ~ 0.4 on day 78 to ~ 27 on day 272, at a phase when the coronal lines were conspicuous. Williams et al. (1996) discussed the possible cause for this after considering the effects of radiative and collisional processes on the observed line ratio R . They found that, between 1250 and 20 000 K, the ratio R is approximately proportional to the temperature (as a consequence of collisional processes playing a dominant role and with the relevant collision strengths having a significant temperature dependence; see their equation 6). They thus suggested that, in the case of nova PW Vul, the large 70-fold increase in R seen between 78 and 272 d after outburst was due partly to the rising temperature in the region where the He/H emission originated. In essence, at least part of the observed behaviour of R is a consequence of the increasing excitation of the nova. This seems to be a viable reason for the later nebular/coronal

stages, when excitation conditions increase in the ejecta. However, for the behaviour observed here – very early after outburst – we offer an alternative explanation. We believe that the He I 1.083- μm line was optically thick on day 9.25 (when $R = 0.31$) and was hence seen at greatly reduced intensity. The electron density at around this time was at least 10^{10} cm^{-3} or greater, as the preceding Case B analysis showed. The emission-line spectrum of neutral helium has been calculated by Almog & Netzer (1989) up to high densities of 10^{14} cm^{-3} . They show that, at densities exceeding 10^{10} cm^{-3} , the He I 1.0830- μm line emissivity and line strength drop dramatically as the optical depth increases (see figs 1 and 3 of Almog & Netzer 1989). Thus by day 28.17, if the ejecta dilutes geometrically with $n_e \propto t^{-2}$ or ballistically with $n_e \propto t^{-3}$, n_e may be expected to reduce by a factor ~ 10 –27 and it is quite possible that the ejecta changes from optically thick to optically thin (or partially thin) conditions between day 9.25 and day 28.17, in which case the line strength should go up considerably, as is indeed seen on day 28.17 when $R = 2.4$.

The second strongest He I line in the NIR region, namely the 2.0581- μm line, also follows a similar behaviour to the 1.083- μm line. Unfortunately, the 2.0581- μm line lies in a window of poor atmospheric transmission due to strong CO₂ absorption, it is considerably weaker than the 1.083- μm line and further it gets veiled as dust formation begins to contribute to the IR excess in that region. As a result, the signal-to-noise ratio (SNR) in this line is low in most of our spectrum, which hampers drawing strong conclusions about its evolution. However, even then, as seen from the last column of Table 5, there is a strong and sudden increase in its strength between days 20 and 28 by more than a factor of 10, with the increased strength tending to persist subsequently. This behaviour is quite similar to that of the 1.083- μm line. However, unlike the 1.0830- μm line, Almog & Netzer (1989) have not analysed the behaviour of the 2.0581- μm line at high densities, so we cannot be sure that we are witnessing optical depth effects here. Generally, the strength of the 2.0581- μm line has been computed mostly at low densities. Benjamin, Skillman & Smits (1999) present line strengths for typical nebular conditions for densities up to $n_e = 10^6 \text{ cm}^{-3}$. We believe there are certain complexities in calculating its line strength at higher densities (R. Porter, private communication); it is not included in the computed strengths of He I lines by Porter et al. (2005).

The question may arise as to why similar behaviour of the He I lines is not seen in other novae. A simple explanation eludes us. However, there are at least two other novae worth discussing, namely recurrent nova T Pyx and V5558 Sgr, where the He I line behaviour, if not identical to this nova, was rather unusual. T Pyx, during its 2011 outburst, showed a significant transition of the nova from the He/N to the Fe II class, from both NIR and optical spectra, within a few days after the outburst (Joshi, Banerjee & Ashok 2014; Ederoclitte 2013). That is, it belonged to the hybrid class of novae (Williams 1992), but with the transition occurring in the reverse direction (He/N to Fe II rather than Fe II to He/N). Prominent He I lines were seen soon after the onset of the eruption, which then faded rapidly in strength within the next few days. A similar behaviour was also seen in the optical in V5558 Sgr (Tanaka et al. 2011). The reason for this phenomenon is not well understood.

3.3.4 Dust formation and evolution

The evolution of the IR spectra is shown in Fig. 9, where an IR excess that builds up with time is clearly seen at longer wavelengths. We attribute this excess to dust emission and model it through

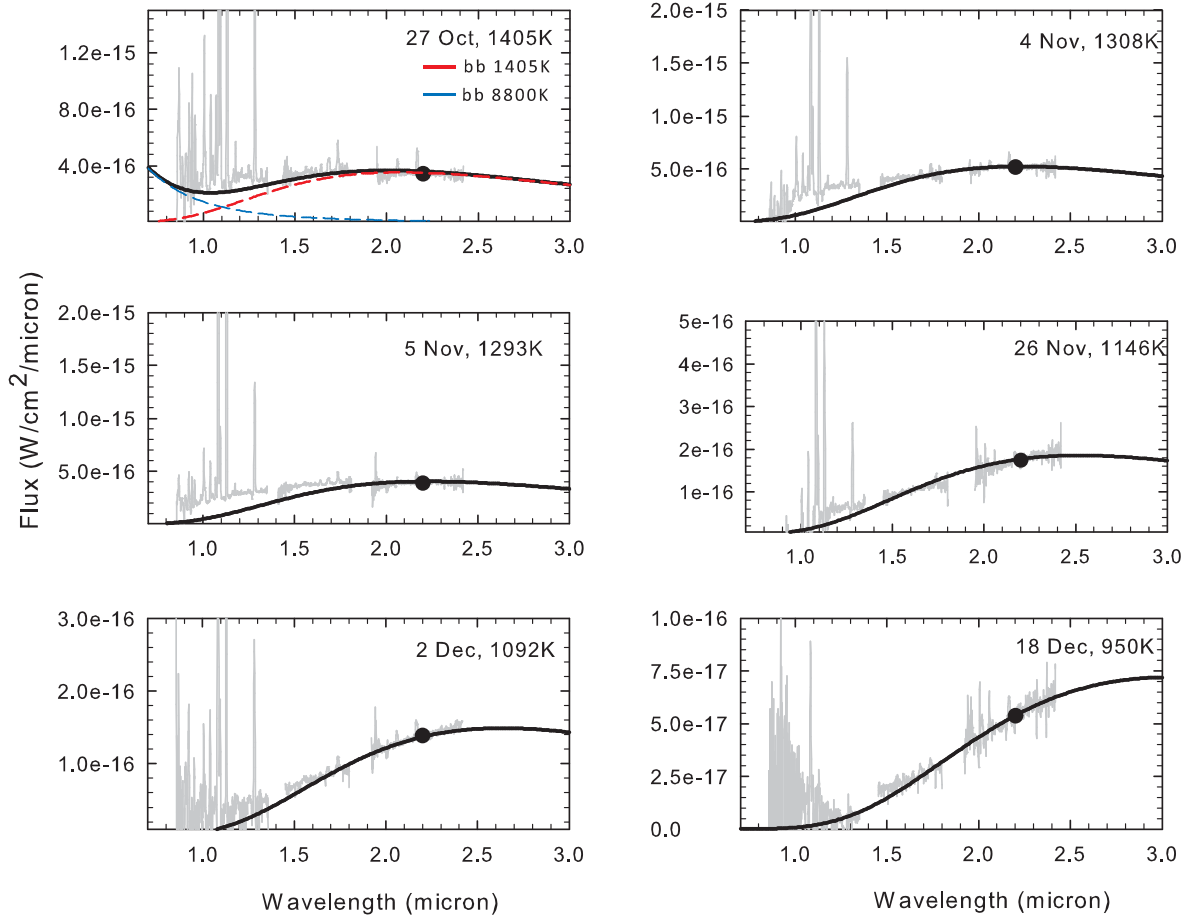


Figure 9. Selected *JHK* spectra (grey) during the dust formation phase, along with their blackbody fits (black) and temperatures. The windows of poor atmospheric transmission between 1.4 and 1.5 μm and 1.8 and 1.95 μm are blanked out. The blackbody fits show a deficit in the *J* band for earlier epochs, which can be accounted for by using an additional contribution from a hotter blackbody at around $\sim 8000\text{--}9000\text{ K}$ from the central remnant. For example, we show the co-added sum (black line) of a two-component Gaussian fit for the data of October 27 in the top left panel, where the hot component (blue dashed line) has an insignificant contribution in the *K*-band region, where the dust blackbody (red dashed line) dominates overwhelmingly.

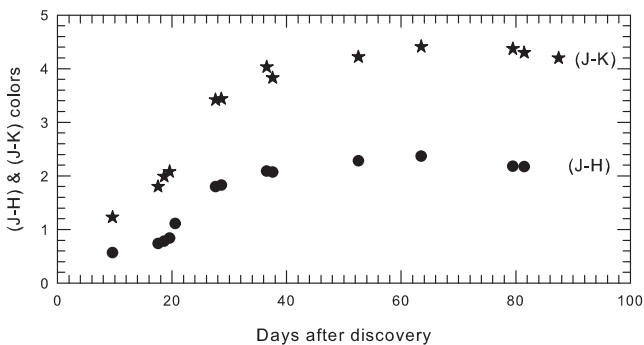


Figure 10. Evolution of the near-infrared (*J* – *H*) and (*H* – *K*) colours with time during the dust formation phase.

blackbody fits. NIR photometry also shows independent supporting evidence for dust formation from the evolution and gradual increase in the (*J* – *H*) and (*J* – *K*) colours during this time (Fig. 10). From Fig. 10, it appears that grain nucleation may have begun even as early as day 17–19 after discovery, because the (*J* – *H*) and (*J* – *K*) colours had already begun to increase at this stage. We show that spectroscopy confirms this. Thus this appears to be a fairly early detection of dust formation in a nova, the earliest

known instance occurring in Nova Her 1991 (V838 Her; Harrison & Stringfellow 1994) at +8 d after outburst. Williams et al. (2013) have analysed the correlation between the dust formation time-scale and the speed class from observational data of CNe and show that dust typically takes longer to form in slower novae. For a t_2 of $\sim 16.5\text{ d}$ as estimated here, a value of approximately 25–27 d for the onset of dust condensation is suggested from their correlation plot. This is in reasonable agreement with the dust condensation time of +19.2 d that we observe, considering that there is statistical scatter in the Williams et al. (2013) correlation plot. What is perhaps more important is the qualitative agreement that, among dust-forming novae, fast novae proceed to form dust quickly.

The blackbody fits for the spectra starting from October 27 (+28 d) are discussed first. The earliest epoch at +19.2 d, when dust formation had just commenced, is discussed and analysed separately later. The blackbody fits of Fig. 9 give good agreement with the observed data at longer wavelengths (namely *K* band), but there is a deficit in the *J* band. We have checked that this deficit can be accounted for by using an additional contribution from a hotter blackbody (at around $\sim 8000\text{--}9000\text{ K}$) from the central remnant. For example, we show a two-component Gaussian fit for the data of October 27 (+28 d) in the top left panel of Fig. 9. As is clearly established, the hot component has insignificant contribution in the *K*-band region, where the blackbody representing the dust emission

Table 6. Dust parameters and their evolution.

t (days)	$(\lambda f_\lambda)_{\max}$ ($10^{-12} \text{ W m}^{-2}$)	T_{dust} (K)	AC^a	Mass ($10^{-8} M_\odot$)		gr. rad a (μm)	
				GR	BB	AC	GR
19.21 ^b	3.49 ± 0.34	1461 ± 15	0.22 ± 0.03	0.34 ± 0.05	0.32 ± 0.04	3.89 ± 0.93	5.83 ± 0.95
28.17	8.35 ± 0.11	1405 ± 27	0.63 ± 0.07	0.96 ± 0.11	0.86 ± 0.08	2.12 ± 0.60	3.23 ± 0.62
36.18	13.10 ± 0.29	1308 ± 14	1.38 ± 0.10	2.20 ± 0.17	1.80 ± 0.12	1.80 ± 0.43	2.87 ± 0.45
37.10	10.12 ± 0.15	1293 ± 23	1.13 ± 0.11	1.81 ± 0.20	1.46 ± 0.13	1.81 ± 0.50	2.90 ± 0.52
58.11	5.23 ± 0.07	1146 ± 42	1.03 ± 0.19	1.77 ± 0.37	1.22 ± 0.20	1.31 ± 0.48	2.24 ± 0.50
59.12	7.62 ± 0.24	1143 ± 38	1.53 ± 0.29	2.62 ± 0.54	1.80 ± 0.29	1.28 ± 0.45	2.20 ± 0.47
64.07	4.39 ± 0.20	1092 ± 31	1.09 ± 0.20	1.92 ± 0.38	1.24 ± 0.20	1.36 ± 0.44	2.38 ± 0.46
80.06	2.64 ± 0.03	950 ± 12	1.27 ± 0.09	2.42 ± 0.19	1.30 ± 0.08	1.68 ± 0.42	3.20 ± 0.43

^aAC = amorphous carbon, GR = graphite, BB = blackbody, gr. rad = grain radius.

^b $(\lambda f_\lambda)_{\max}$ and mass estimates for this epoch are upper limits.

dominates overwhelmingly. As a consequence of this, we are justified in neglecting the contribution from the hot component and we deem it sufficient to give primary importance to the K -band data while arriving at best fits for the dust emission to estimate the dust temperature. The best fits were obtained using a standard least-squares minimization Marquardt–Levenberg algorithm; the formal errors are small because of the large number of points in the K band that are being fitted. A limitation of this work is the lack of data at longer mid-IR wavelengths, which would have given a more extended SED and more reliable estimates of the dust temperature.

The dust temperature and the $(\lambda f_\lambda)_{\max}$ values are listed in Table 6. Using these, we estimate how optically thick the dust was by comparing the dust and outburst luminosities. Given that the integrated flux under a blackbody curve is given by $1.35(\lambda f_\lambda)_{\max}$ (Gehrz & Ney 1992), we have the maximum dust luminosity $L_{\text{IR}} = 1.2 \times 10^4 L_\odot$ on day 36.37 using $(\lambda f_\lambda)_{\max}$ from Table 6. The outburst luminosity is estimated from $M_{\text{bol}} = 4.8 + 2.5 \log(L/L_\odot)$, where the bolometric correction applied to M_V is assumed to lie between -0.4 and 0.00 , corresponding to A–F spectral types, respectively (novae at maximum generally have a spectral type between A and F). Using $M_V = -8.29$ as deduced previously, the outburst luminosity L_0 is then $(2.11 \pm 0.38) \times 10^5 L_\odot$, which is approximately 6–7 times the Eddington luminosity for a $1-M_\odot$ white dwarf. We adopt a mean value of $2.11 \times 10^5 L_\odot$ for the outburst luminosity in subsequent calculations. In comparison, the dust luminosity L_{IR} is significantly less, with L_{IR}/L_0 being ~ 0.06 , indicating that very little of the central engine’s optical/UV output radiation is intercepted, absorbed and reprocessed into IR emission. This would imply that the dust could be clumpy and hence would not cover all angles of the sky towards the nova as seen by the observer. Alternatively, the dust shell may be homogenous but having insufficient material to be optically thick, i.e. it does not behave as an ideal calorimeter that traps all radiation. The few points available in the V -band light curve between 2015 November 10 and 20 (at a time when dust was present) have large error bars, but still do not show any hint of a strong dip in optical brightness, as expected for an optically thick dust-forming event, e.g. similar to the deep dips in the dust-forming events in V705 Cas (Evans et al. 1996), V5668 Sgr (Banerjee et al. 2016) or a few other D-type (dust type) novae catalogued in Strope, Schaefer & Henden (2010).

The behaviour here is similar to that of two other optically thin dust-forming novae, Nova Cyg 2006 (Munari et al. 2008) and V2615 Oph (Das et al. 2009). In the former nova, Munari et al. (2008) found that the optical depth of the dust reached 0.2, with no measurable effects on the light curve at optical wavelengths but displaying, however, a large increase in the JHK magnitudes. The mass of the ejecta was estimated as $5 \times 10^{-4} M_\odot$ from [O I] lines and

$3 \times 10^{-4} M_\odot$ from CLOUDY modelling, while the IR emission from dust suggested that $M_{\text{gas}}/M_{\text{dust}} = 3 \times 10^5$.

3.3.5 Dust mass and grain size

To estimate the dust mass, it is assumed that the grains are spherical with mean radius a and that the dust is composed of carbonaceous material. The justification for the carbon composition is discussed briefly. Based on the mean Planck absorption efficiencies $\langle Q_{\text{abs}} \rangle$ for carbon grains provided by Blanco, Falcicchia & Merico (1983), Evans et al. (2017) have shown that $\langle Q_{\text{abs}} \rangle$ can be approximated well by a form $\langle Q_{\text{abs}} \rangle = Aa^\gamma T^\beta$. They find that the Planck mean absorption efficiencies from Blanco et al. (1983) are very well fitted by the relations $\langle Q_{\text{abs}} \rangle/a = 53.160T^{0.754}$ and $\langle Q_{\text{abs}} \rangle/a = 0.653T^{1.315}$ for amorphous carbon (AC) and graphitic (GR) grains, respectively, with a in cm and T in Kelvin. The fit for the AC grains is excellent over the temperature range 400–1700 K, while for graphitic carbon the fit is reasonably satisfactory over the range 700–1500 K (i.e. over the range of dust temperatures seen here in V1831 Aql; refer to Table 6). For blackbody grains, $A = 1$ and $\beta = \gamma = 0$. Using these relations, it can be shown (Evans et al. 2017) that the dust masses for AC, GR and blackbody grains are given as follows.

For optically thin amorphous carbon,

$$\frac{M_{\text{dust-AC}}}{M_\odot} \simeq 6.91 \times 10^{17} \frac{(\lambda f_\lambda)_{\max}}{T_{\text{dust}}^{4.754}}, \quad (5)$$

and for optically thin graphitic carbon,

$$\frac{M_{\text{dust-GR}}}{M_\odot} \simeq 6.16 \times 10^{19} \frac{(\lambda f_\lambda)_{\max}}{T_{\text{dust}}^{5.315}}, \quad (6)$$

if the grains behave as perfect blackbodies,

$$\frac{M_{\text{dust-bb}}}{M_\odot} = 4.02 \times 10^{15} \frac{a(\lambda f_\lambda)_{\max}}{T_{\text{dust}}^4}, \quad (7)$$

where a value of $D = 6.1$ kpc has been used for the distance, $\rho = 2.25 \text{ gm cm}^{-3}$ has been taken as the density of the carbon grains, grain radius $a = 1 \mu\text{m}$ is assumed for the blackbody dust mass relation and $(\lambda f_\lambda)_{\max}$ is in units of W m^{-2} . Estimated dust masses are tabulated in Table 6 using the T_{dust} values listed therein. It must be noted that the entry in Table 6 at 19.2 d for the temperature is not estimated from a blackbody fit, but slightly differently; this procedure is now described. It is first established that a mild but definite IR excess was present at 19.2 d that was not present in the first spectrum of +9.2d. The top panel of Fig. 11 shows the spectra for days +9.2 and +19.2, with the spectrum of day 19.2 scaled upwards to match the spectrum of 9.2d in the J band. As a consequence of this exercise, a clear IR excess is seen to have

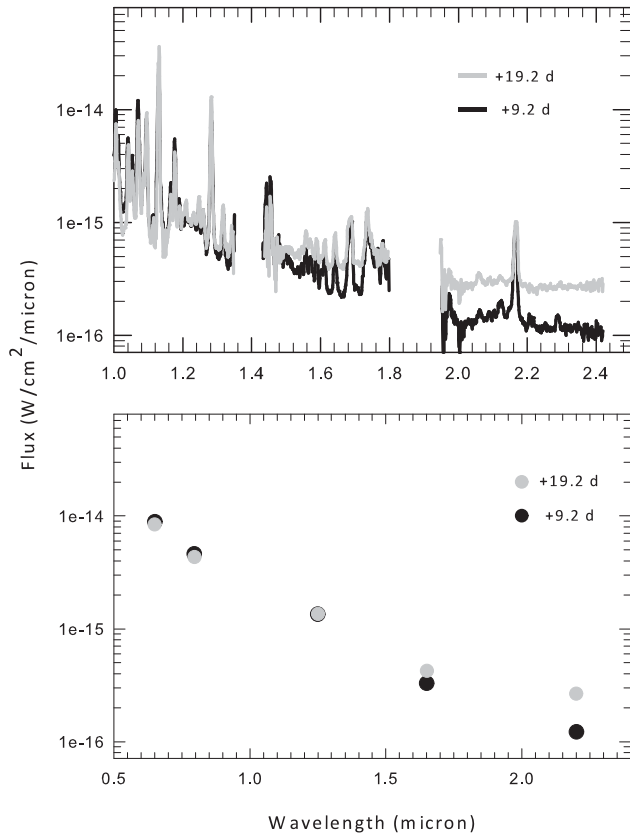


Figure 11. Top panel: changes seen in the spectra between days 9.2 and 19.2, showing the development in the latter epoch of an infrared excess in the H and K bands due to dust. Bottom panel: the IR excess developing on day 19.2, shown using R_c , I_c , J , H , K_s broad-band photometry. In both panels, the spectra and photometric fluxes of days 9.2 and 19.2 have been scaled so as to match each other in the J band. More details are given in the text.

newly developed in the H and K bands. The same conclusion is also reached by plotting the dereddened R_c , I_c , J , H , K_s fluxes from this article for days 9.2 and 19.2 in the bottom panel. The J -band fluxes of both days have been matched after scaling. A newly developed IR excess is seen in the H and K bands, while the fluxes in all other bands match well, indicating the nova has faded reasonably similarly in these bands. It is clear that dust has begun to contribute to the SED on day 19.2. It is not meaningfully possible to fit a blackbody to this dust excess to estimate the dust temperature without causing substantial errors, because the excess is mild and the contribution of the hot central remnant (as discussed earlier) to the K band is uncertain, but could be significant. We thus estimate the dust temperature for +19.2 d to be 1461 ± 15 K, from extrapolation of the linear best fit to the dust evolution curve shown in the middle panel of Fig. 12. An upper limit on the dust flux can be set by assuming that the entire K -band flux for day +19.2 is due to dust emission, in which case a blackbody curve at 1461 K drawn to match the K -band flux level of 19.2 d yields a value of $(\lambda f_\lambda)_{\max} = 3.49 \times 10^{-12}$ W m $^{-2}$, which is listed in Table 6. This value of $(\lambda f_\lambda)_{\max}$ and also the mass estimate derived from it using equations (5)–(7) are upper limits and are indicated as such in Table 6.

Regarding the choice of carbon for the dust composition, Lodders & Fegley (1995, 1999) have shown that the condensation temperature of different minerals is very much dependent on

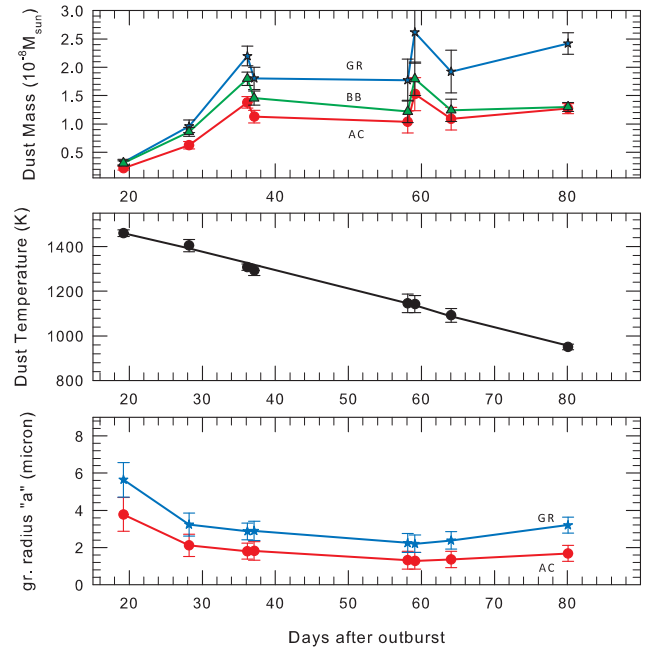


Figure 12. Evolution of the dust mass, temperature and grain radius with time. A detailed discussion of the evolution of these parameters has been made in the text. AC = amorphous carbon, GR = graphite and BB = blackbody.

the C/O ratio, the gas pressure and elemental abundances. However, most estimates show that the condensation temperature for carbon dust (both amorphous and graphite) is high and lies in a range between 1600 and 1800 K in most astronomical environments such as the interstellar medium (ISM: Blanco et al. 1983), Type II supernovae (Todini & Ferrara 2001) or C-rich stellar environments of M and N stars (Lodders & Fegley 1995, 1999). Condensation temperatures for graphite may even exceed 1800 K under certain conditions (Lodders & Fegley 1995). The above-mentioned studies similarly show that most silicates condense at lower temperatures between 1100 and 1400 K (Todini & Ferrara 2001; Speck et al. 2000; Lodders & Fegley 1995, 1999). The dust temperature at the first epoch of 1461 K is too high to favour a silicate composition, but consistent with a carbonaceous constitution. A carbon composition is also consistent with the presence of numerous strong lines of neutral C I, as seen in the NIR spectra in Fig. 7. The treatment of a Si-rich composition is beyond the scope of this work.

Similar temperatures for the dust to those observed here, or higher, have been estimated in several novae, especially when the dust emission was detected early due to monitoring at high cadence. For example, a temperature of 1615 K was detected in the Fe II nova V476 Scuti (Das, Banerjee & Ashok 2013), which might have eluded detection had the observation been untimely, since the dust rapidly cooled to 1040 K within 24 d. The first dust detection in nova V339 Del was at 1637 K (Evans et al. 2017) and temperatures in the range 1300–1700 K were estimated in V1280 Sco at different stages of the dust evolution (Chesneau et al. 2008), while the dust in the classical nova V2326 Cyg condensed at a temperature of 1410 ± 15 K (Lynch et al. 2008). A condensation temperature as high as 1800 K is suggested in the helium nova V445 Puppis (Ashok & Banerjee 2003). V445 Puppis is of course an exceptional nova; it was the slowest among the dust-forming novae, as can be seen from its isolated position in the speed versus dust formation time-scale plot of Williams et al. (2013). The dust

shell, which formed initially in early 2001, is extremely dense, with the object continuing to remain cocooned in dust even today, as we find from regular monitoring by us from Mount Abu (and also in a private communication from Dr Patrick Woudt).

The grain size can be calculated by equating the fraction of the outburst luminosity intercepted by the grains and subsequently re-emitted in the IR, which is observationally a known quantity. This leads to the following relation for the grain radius (Gehrz et al. 1980, 2017; Evans et al. 2005):

$$a = \frac{L_O}{16\pi AR^2\sigma T^{(\beta+4)}}, \quad (8)$$

where R is the nova-to-grain distance at a time t , assumed to be given by $v \times t$ where v is the velocity, L_O is the outburst luminosity and σ is the Stefan–Boltzmann constant. L_O is assumed to remain constant, as would be expected for a CN during the evolutionary phase discussed here. A value of $v = 650 \text{ km s}^{-1}$ is adopted using the HWHM of the H α profile of Fig. 6 in Section 3.2. The computed grain sizes for AC and GR grains are listed in Table 6 and also shown in Fig. 12. From Fig. 12 (top panel), a large increase by a factor of 6 is seen in dust mass between the first and third epochs (+19.21–36.18 d), corresponding to considerable growth in the number of grains subsequent to grain nucleation. Keeping in mind that the mass estimates of day +19.2 are upper estimates, the increase in mass during this period is expected to be more than sixfold. This growth period is followed by a phase where the mass remains fairly constant over the remaining course of the observations, indicating neither significant growth nor destruction of the grains.

Apart from sputtering and chemi-sputtering processes, which can cause grain destruction (Evans et al. 2017 and references therein), X-ray emission from the hot central white dwarf (WD) can be responsible for dust destruction, principally by grain heating and grain charging (Fruchter, Krolik & Rhoads 2001). Grain charging, which can lead to electrostatic stresses building up within a grain that are greater than the grain’s tensile strength, is often the more important mechanism for destruction (Fruchter et al. 2001). Nova V339 Del, for example, passed through a long supersoft phase (SS) and the X-ray radiation, as shown by Evans et al. (2017), could have been responsible for dust destruction. However, in the case of the present nova there were no reports of the detection of any X-ray emission from it. Even if it did pass through an X-ray emission phase, the possibility still remains that the grains could have been shielded from destruction by residing in dense clumps or regions of high density (this is discussed further below), into which the hard radiation could not penetrate fully. However, observations taken recently on 2016 October 12 using deep exposures failed to detect the nova up to limiting magnitudes of $J = 16.5$ and $K = 14.75$. It is possible that the dust has been destroyed by this stage or its emission has dropped below detection limits. Alternatively, it could still have been present, but the dust SED may have shifted to longer wavelengths.

The middle panel of Fig. 12 shows the cooling of the dust with time, which is well approximated by a linear relation $T = 1619.6289 - 8.2699 \times t$, where t is the time (this is a least-squares minimized fit). This fit, which excluded the first data point, was used to extrapolate and estimate a dust temperature of 1461 ± 15 on day 19.2 (the first data point), which is listed in Table 6 and was used to estimate the dust mass on that day.

The bottom panel shows the evolution of the grain radius with time. Surprisingly, the grain radius shows an initial decrease followed by an almost constant or mildly increasing trend. The latter behaviour implies that the destructive processes that could reduce

grain size are absent, e.g. grain sputtering or grain shattering due to hard radiation. A similar inference was reached earlier from the evolution of the dust mass. The decrease in radius is hard to explain, because grains are expected to grow in size after the initial nucleation phase. A plausible reason for this decrease could lie in the simple assumptions behind equation (8) used to determine grain radius. A spherical geometry has been assumed and the dust shell radius is assumed to evolve linearly with time, following $R = v \times t$. However, high-resolution spatial observations using either adaptive optics or interferometry show that the bipolar shape is fairly common in novae. In fact, time may show – as has been the case for planetary nebulae (PNe) – that the bipolar shape may be the generalized shape that most CNe possess during the early expansion stages. Examples of bipolar morphology in the early stages are established clearly, either through direct imaging or interferometry, in V445 Puppis (Woudt et al. 2009), RS Oph (O’Brien et al. 2006), V1280 Sco (Chesneau et al. 2012), Nova Mon 2012 (Chomiuk et al. 2014) and V339 Del (Schaefer et al. 2014). There are old nova remnants too like HR Del that have retained the bipolar morphology long after the original outburst.

A tacit expectation of spherical morphology was perhaps the norm for PNe until the interacting winds scenario, proposed by Kwok, Purton & Fitzgerald (1978), and subsequent elaborate and rigorous models developed by other workers (Balick & Frank 2002 and references therein) showed that the hourglass (or equivalently the bipolar shape) could be generated easily in the interacting winds scenario, with spherical morphology being just one special subclass. The generic requirement to generate such a bipolar morphology was a density enhancement at the equatorial region (e.g. caused by matter concentrated in the equatorial regions that is left over from the common envelope phase), which restricts the wind (or nova ejecta) from expanding freely in the equatorial direction but allows an easy flow in the polar direction. Matter at the poles is then expected to expand very rapidly, while that in the equatorial waist is expected to expand very slowly, thereby creating different expansion velocities across the bipolar structure. An example of this may be seen from the kinematics of the ejecta in the nova V455 Pup (fig. 6 of Woudt et al. 2009), wherein the equatorial matter at the waist barely expands with time. The nova under study here may also have similar kinematical behaviour. The double-peaked velocity profile in Fig. 6 indicates that there is a departure from spherical symmetry in the ejecta flow and a bipolar flow cannot be ruled out. Thus this nova may have an equatorial density enhancement, which additionally may be the site where the bulk of the dust resides. This is quite likely, because such regions, by virtue of being dense, are likely to have the critical density (Gehrz 1988) needed for grain nucleation to occur, while also being shielded from hard radiation that could potentially cause dust destruction. If such circumstances exist in this nova, then equation (8) suggests that it is difficult to assign precise meaning or values to the terms R or v .

There are other complexities that affect the precise determination of the kinematics. First, the velocity of the flow could change significantly between epochs. Observations that probed the nova’s spatial development at very high resolution were not available earlier. Now, however, this is clearly seen from interferometric observations of V339 Del, which show that there are considerable changes in the expansion rate with time (Schaefer et al. 2014). Especially relevant during the dust formation stage is the sharp drop in velocity immediately after dust onset, followed immediately thereafter by a rapid increase in the expansion rate (fig. 2 of Schaefer et al. 2014). The second complexity is in the varying locations of the dust sites (hence

giving rise to different R values). For example, apart from showing that dust emission emanates from all across the nova, V1280 Sco showed preferential and enhanced dust concentrations in the polar caps. All these factors above render it difficult to assign a unique definition to the radius R in equation (8) or to justify the simple assumption that $R = v \times t$, as we have used here. We feel these simple assumptions can lead to imprecision in the results and the decrease in grain radius seen in the initial two epochs could be a consequence of this. However, it is felt that the principal result from this analysis is that the grain radii determined here for both amorphous and graphitic grains are typically of the order of a micron or slightly more. This is similar to what is found in other novae when using the same formalism as adopted here (Gehrz et al. 1980; Gehrz 1988; Evans et al. 2017).

4 SUMMARY

Multi-epoch near-infrared and optical photometric and spectroscopic observations are presented for nova V1831 Aquilae (Nova Aquilae 2015), discovered in outburst on 2015 September 9. We demonstrate that NIR spectroscopy is self-contained to establish whether a nova is of the Fe II or He/N class; in this particular case, V1831 Aql is shown to be of the Fe II class. The distance and extinction A_v to the nova are estimated to be 6.1 ± 0.5 kpc and ~ 9.02 mag, respectively. From a Case B analysis of the optically thick hydrogen Brackett lines, the lower limits on the electron density n_e and ejecta mass are found to be in the range $\sim 5 \times 10^9 - 1.2 \times 10^{10} \text{ cm}^{-3}$ and $(2.4-5.7) \times 10^{-6} M_\odot$, respectively. From [O I] line ratios, we estimate the neutral oxygen temperature and mass to be $T_e = 5156 \pm 170$ K and $M_{\text{O I}} = (8.8 \pm 2.2) \times 10^{-5} M_\odot$, respectively. A rapid, approximately 10–15 fold increase is seen in the $(\text{He I } 1.083)/(\text{Pa}\gamma \text{ } 1.094)$ line ratio during the early stages of evolution. This possibly arises due to the He I line transitioning from an optically thick to an optically thin state as the ejecta expands and dilutes. Dust formation is found to occur in V1831 Aql around 19.2 d after discovery at a condensation temperature of 1461 ± 15 K, following which the dust gradually cools down to 950 K over a period of ~ 50 d. Based on the condensation temperature, we suggest a carbonaceous composition for the dust. The dust mass shows a significant increase following nucleation, by more than a factor of six between +19.21 and 36.18 d, which is best interpreted as being due to considerable growth in the number of grains. This growth period is followed by a phase where the mass remains fairly constant over the remaining course of the observations, indicating neither significant growth nor destruction of the grains. Following nucleation, the grains, instead of showing growth, show a decrease in radii during the initial stages. The plausible reasons for this behaviour and the subsequent evolution of the grain size are discussed.

ACKNOWLEDGEMENTS

The research work at the Physical Research Laboratory is funded by the Department of Space, Government of India. We thank A. Frigo, P. Ochner, S. Dallaporta and U. Sollecchia for their assistance with some of the optical observations. We acknowledge the use of data from the AAVSO data base.

REFERENCES

Almog Y., Netzer H., 1989, MNRAS, 238, 57
Ashok N. M., Banerjee D. P. K., 2003, A&A, 409, 1007

- Ashok N. M., Srivastava M. K., Banerjee D. P. K., 2015, Astron. Telegram, 8142, 1
Balick B., Frank A., 2002, ARA&A, 40, 439
Banerjee D. P. K., Ashok N. M., 2002, A&A, 395, 161
Banerjee D. P. K., Ashok N. M., 2012, Bull. Astron. Soc. India, 40, 243
Banerjee D. P. K., Ashok N. M., Venkataraman V., 2012, Astron. Telegram, 4542, 1
Banerjee D. P. K., Srivastava, Mudit K., Ashok N. M., Venkataraman V., 2016, MNRAS, 455(1), L109
Benjamin R. A., Skillman E. D., Smits D. P., 1999, ApJ, 514, 307
Blanco A., Falcicchia G., Merico F., 1983, Ap&SS, 89, 1638
Cardelli J. A., Clayton G. C., Mathis J., 1989, ApJ, 345, 245
Chesneau O. et al., 2008, A&A, 487, 223
Chesneau O. et al., 2012, A&A, 545, 63
Chomiuk L. et al., 2014, Nature, 514, 339
Das R. K., Banerjee D. P. K., Ashok N. M., Chesneau O., 2008, MNRAS, 391, 1874
Das R. K., Banerjee D. P. K., Ashok N. M., 2009, MNRAS, 398, 375
Das R. K., Banerjee D. P. K., Ashok N. M., Mondal S., 2013, Bull. Astr. Soc. India, 41, 195
della Valle M., Livio M., 1995, ApJ, 452, 704
Della Valle M., Pasquini L., Daou D., Williams R. E., 2002, A&A, 390, 155
Downes R. A., Duerbeck H. W., 2000, AJ, 120, 2007
Ederoclite A., 2013, in Guirado J. C., Lara L. M., Quilis V., Gorgas J., eds, Highlights of Spanish Astrophysics VII, Proceedings of the X Scientific Meeting of the Spanish Astronomical Society (SEA), held in Valencia, 2012 July 9–13, pp. 539–542.
Evans A., Geballe T. R., Rawlings J. M. C., Scott A. D., 1996, MNRAS, 282, 1049
Evans A., Tyne V. H., Smith O., Geballe T. R., Rawlings J. M. C., Eyres S. P. S., 2005, MNRAS, 360, 1483
Evans A. et al., 2017, MNRAS, 466, 4221
Fruchter A., Krolik J. H., Rhoads J. E., 2001, ApJ, 563, 597
Fujii M., 2015, IAU Circ., 9278, 1
Gehrz R. D., 1988, ARA&A, 26, 377
Gehrz R. D., Ney E. P., 1992, Icarus, 100, 162
Gehrz R. D., Hackwell J. A., Grasdalen G. I., Ney E. P., Neugebauer G., Sellgren K., 1980, ApJ, 239, 570
Gehrz R. D. et al., 2015, 812, 132
Gehrz R. D. et al., 2017, ApJ, submitted
Goranskij V. P., Barsukova E. A., 2015, Astron. Telegram, 8150, 1
Harrison T. E., Stringfellow G. S., 1994, ApJ, 437, 827
Hummer D. G., Storey P. J., 1987, MNRAS, 224, 801
Joshi V., Banerjee D. P. K., Ashok N. M., 2014, MNRAS, 443, 559J
Kwok S., Purton C. R., Fitzgerald P. M., 1978, ApJ, 219, L125
Landolt A. U., 2009, AJ, 137(5), 4186
Lodders K., Fegley B., Jr, 1995, Meteoritics, 30, 661
Lodders K., Fegley B. Jr, 1999, in Le Bertre T., Lebre A., Waelkens C., eds, IAU Symp. 191, Asymptotic Giant Branch Stars, p. 279
Lynch D. K. et al., 2008, AJ, 136, 1815
Maccarone T. J., 2015, Astron. Telegram, 8136, 1
Maehara H., Fujii M., 2015, Astron. Telegram, 8127, 1
Marshall D. J., Robin A. C., Reyle C., Schultheis M., Picaud S., 2006, A&A, 453, 635
McLaughlin D. B., 1960, in Greenstein J. L., ed., Stellar Atmospheres. Univ. Chicago Press, Chicago
Munari U., Moretti S., 2012, Baltic Astron., 21, 22
Munari U. et al., 2008, A&A, 492, 145
Munari U. et al., 2012, Baltic Astron., 21, 13
Munari U., Maitan A., Moretti S., Tomaselli S., 2015, New Astron., 40, 28
Naik S., Banerjee D. P. K., Ashok N. M., Das R. K., 2010, MNRAS, 404, 367
Nakano S., 2015, IAU Circ., 9278, 1
O'Brien T. J. et al., 2006, Nature, 442, 279
Payne-Gaposchkin C., 1957, The Galactic Novae. North-Holland Publishing Co., Amsterdam
Pontefract M., Rawlings J. M. C., 2004, MNRAS, 347, 1294

- Porter R. L., Bauman R. P., Ferland G. J., MacAdam K. B., 2005, *ApJ*, 622, L73
- Rieke G. H., Levofsky M. J., 1985, *ApJ*, 368, 468
- Schaefer G. H. et al., 2014, *Nature*, 515, 234
- Schlafly E., Finkbeiner D. P., 2011, *ApJ*, 737, 103
- Shafter A. W. et al., 2011, *ApJ*, 734, 12
- Shappee B. J. et al., 2015, *Astron. Telegram*, 8126, 1
- Speck A. K., Barlow M. J., Sylvester R. J., Hofmeister A. M., 2000, *A&AS*, 146, 437
- Srivastava M. K., Banerjee D. P. K., Ashok N. M., 2015a, *Astron. Telegram*, 8332, 1
- Srivastava M., Ashok N. M., Banerjee D. P. K., Sand D., 2015b, *MNRAS*, 454, 1297
- Stanek K. Z., 1996, *ApJ*, 460, L37
- Storey P. J., Hummer D. G., 1995, *MNRAS*, 272, 41
- Strope R. J., Schaefer B. E., Henden A. A., 2010, *AJ*, 140, 34
- Tanaka J., Nogami D., Fujii M., Ayani K., Kato T., Maehara H., Kiyota S., Nakajima K., 2011, *PASJ*, 63, 911
- Todini P., Ferrara A., 2001, *MNRAS*, 325, 726
- van den Bergh S., Younger P. S., 1987, *A&AS*, 70, 125
- Warner B., 1995, in *Cataclysmic Variable Stars*, *Camb. Astrophys. Ser.*, Vol. 28. Cambridge Univ. Press, Cambridge
- Williams R. E., 1992, *AJ*, 104, 725
- Williams R. E., 1994, *ApJ*, 426, 279
- Williams R. E., 2012, *AJ*, 144, 98
- Williams R. E., Hamuy M., Phillips M. M., Heathcote S. R., Wells L., Navvarete M., 1991, *ApJ*, 376, 721
- Williams P. M., Longmore A. J., Geballe T. R., 1996, *MNRAS*, 279, 804
- Williams S. C., Bode M. F., Darnley M. J., Evans A., Zubko V., Shafter A. W., 2013, *ApJ*, 777, L32
- Woudt P. A. et al., 2009, *ApJ*, 706, 738

This paper has been typeset from a \TeX/L\AA\TeX file prepared by the author.